RESEARCH ARTICLE | AUGUST 05 2025

Impacts of ventilation layouts on dust dispersion and particulate exposure in deep mining: A study within a full-scale heading face

Jiaqi Fan ; Xueren Li ; Ruipeng Xu; Zhaoxing Li; Changgeng Gui; Shihang Li ; Zhengbiao Peng; Fan Geng ; Xinjian He

Physics of Fluids 37, 083321 (2025)
https://doi.org/10.1063/5.0276290

Physics of Fluids ARTICLE pubs.aip.org/aip/pof

Impacts of ventilation layouts on dust dispersion and particulate exposure in deep mining: A study within a full-scale heading face

Cite as: Phys. Fluids **37**, 083321 (2025); doi: 10.1063/5.0276290
Submitted: 17 April 2025 · Accepted: 26 June 2025 ·
Published Online: 5 August 2025

View Online Export Citation CrossMark

Jiaqi Fan,[1,2] Xueren Li,[1,2,3] Ruipeng Xu,[4] Zhaoxing Li,[5] Changgeng Gui,[1,2] Shihang Li,[1,2] Zhengbiao Peng,[1,2] Fan Geng,[2,6,a)] and Xinjian He[1,2,a)]

AFFILIATIONS

[1]School of Safety Engineering, China University of Mining and Technology, Xuzhou 221116, China
[2]Jiangsu Engineering Research Center of Dust Control and Occupational Protection, Xuzhou 221008, China
[3]School of Engineering, RMIT University, PO Box 71, Bundoora, Victoria 3083, Australia
[4]Department of Chemical Engineering, Faculty of Applied Sciences, Delft University of Technology and J.M. Burgerscentrum Research School for Fluid Mechanics, Van der Maasweg 9, 2629 HZ Delft, The Netherlands
[5]School of Chemical Engineering and Technology, China University of Mining and Technology, Xuzhou 221116, China
[6]School of Low-Carbon Energy and Power Engineering, China University of Mining and Technology, Xuzhou 221116, China

[a)]**Authors to whom correspondence should be addressed:** gengfan0104@163.com and xinjian.he@cumt.edu.cn

ABSTRACT

Deep coal mining operates in increasingly extreme environments, where substantial dust generated during the mining process poses serious risks to both production safety and miners' health. To understand the dust transport pattern and miners' particulate exposure risk within a full-scale heading face under various ventilation configurations, airflow patterns and dust dispersion characteristics were systematically investigated using the Euler–Lagrangian approach. A user-defined function was developed to enable the dynamic injection of particles, simulating realistic dust generation processes. The average residence times of particles with varying sizes were calculated, and the number of particles entering the respiratory zone was quantified to assess the driver's exposure risk. Results revealed that the driver remained in the recirculation zone in all layouts. The centrally positioned ventilation cylinder facilitated the suspension of smaller particles. With a total suspension time of 300 s and an air supply velocity of 11 m/s, particles sized below 20 μm exhibited the longest average residence time—11.24% and 26.24% longer than in layout R (cylinder on the opposite side of the driver) and layout L (cylinder on the driver's side), respectively. Smaller respiratory dust (i.e., $d_p < 7.07$ μm) and particles originating from the upper part of the dust injection surface were most likely to enter the driver's respiratory zone. Increasing the fresh air supply alone proved insufficient to reduce particulate exposure. Among the configurations, layout L was optimal, reducing particulate exposure by 65.12% compared to layout R. This study provides theoretical insights for optimizing ventilation strategies within the heading face.

I. INTRODUCTION

As one of the most abundant and cost-effective energy sources, coal has long played a fundamental role in global energy systems.[1] Despite the increasing adoption of renewable energy, many economies, particularly those with high energy demands and rapid industrial growth, continue to partially depend on coal to maintain a stable energy supply. China exemplifies this trend. According to the China Mineral Resources Report, the total primary energy production in 2023 reached 4.83×10^9 tons of standard coal with coal contributing 66.6% of this total. In the same year, coal production amounted to 4.71×10^9 tons, marking a 3.4% year-on-year increase.[2] These figures demonstrate that coal remains the primary energy source in China's energy structure, and this pattern is unlikely to undergo significant changes in the short term. As such, coal will continue to serve as the "ballast" and "stabilizer" of the energy system, ensuring the security and stability of the national energy supply.

Recently, the growing demand for coal resources has spurred the rapid development of the coal mining industry.[3] In China, underground mining is the primary method of coal extraction, with underground coal mines accounting for approximately 92% of the total,

significantly outnumbering open-pit mines.[4] However, as shallow coal reserves continue to deplete, mining operations are progressively extending to greater depths. An increasing number of mines are now operating at depths exceeding 800 m, resulting in progressively harsher underground working conditions.[5–8] Deep mining not only faces severe thermal damage issues, as research has shown that for every 100-m increase in mining depth, the downhole temperature rises by 2–4 °C[9,10] but is also accompanied by the release of groundwater, resulting in a significant increase in humidity.[11] More critically, the generated dust during deep mining is difficult to control in the confined underground environment, thereby exacerbating dust pollution. This issue is particularly pronounced within the heading face, i.e., the working area where new roadways are excavated in underground coal mines. Without dust control measures, dust concentrations within the heading face can reach 1000–3000 mg/m^3,[12] making it one of the most heavily dust-polluted areas in underground mining.[13]

The high-concentration dust generated during the mining process not only poses significant risks to the safe production of coal mines but also seriously threatens the health of miners.[14,15] As a highly flammable substance, coal dust presents a substantial explosion hazard in confined spaces when concentrated at high levels. Statistics indicate that 87.32% of China's 532key coal mines are confronted with coal dust explosion risks.[16] Additionally, elevated dust concentrations impair light transmission, reducing miners' visibility and increasing the likelihood of operational errors,[17,18] thus increasing safety hazards during the production process. Furthermore, prolonged exposure to high dust concentrations inevitably leads to excessive dust inhalation. Smaller dust particles can penetrate deep into the lungs and reach the alveolar region, where they irritate lung tissue and induce chronic inflammatory reactions.[19,20] Prolonged inhalation of coal dust can lead to lung fibrosis and respiratory failure, ultimately resulting in pneumoconiosis.[21,22] By the end of 2021, China had reported a cumulative total of 915 000 cases of occupational pneumoconiosis,[23] with coal workers' pneumoconiosis accounting for more than half of these cases.[24,25] Therefore, effective dust control strategies are urgently needed to mitigate dust pollution, ensuring both the safe extraction of coal and protecting miners' lifelong health.

To reduce dust pollution within the heading face, wet dust suppression techniques, such as coal seam water injection and dust suppression sprays, have been widely employed in coal mines.[26–28] While these methods improve the operating environment to some extent, they also exacerbate the high humidity within the heading face. Currently, ventilation is one of the primary and most effective methods for controlling dust in underground coal mines, effectively preventing dust accumulation.[25,29]

In recent years, numerous systematic studies have been conducted on ventilation and dust suppression within the heading face. Nie *et al.*[30] established a simulated experimental system for the heading face and investigated the effects of various ventilation parameters on airflow and dust migration under the long-pressure short-extraction ventilation method. Building on this experimental system, they subsequently designed and developed a novel multi-radial vortex wind generator.[31] Additionally, Ren *et al.*[32] designed a dust suppression device specifically for underground tunneling and validated its effectiveness through field tests. Zheng *et al.*[33] experimentally investigated the impact of ventilation speed, ventilation cylinder position, driver height, and other factors on dust concentration around the driver and pedestrians.

Despite these advancements, there are certain limitations to experimental studies, as it is challenging to obtain detailed data on the airflow and particle diffusion and distribution within the heading face through direct measurements. The complex and dynamic underground environment poses significant challenges to on-site data collection. Additionally, constructing a full-scale simulation platform in the laboratory is costly. Consequently, many researchers are turning to cost-effective numerical simulation methods for more detailed analyses. Hu *et al.*[34] investigated the influence of air supply velocity on dust diffusion in excavation roadways by the computational fluid dynamics-discrete phase model (CFD-DPM). To better account for the interactions between dust particles, Geng *et al.*[35,36] conducted studies on the diffusion characteristics of dust pollutants within the heading face under hybrid and forced ventilation based on the computational fluid dynamics-discrete element method (CFD–DEM). Wang *et al.*[37] analyzed the dispersion characteristics of respirable dust within the heading face and put forward improvements to existing ventilation layouts, achieving a removal efficiency exceeding 90% for respirable dust. Recently, Yu *et al.*[38–40] introduced a large vortex flow technology, employing zoned ventilation to control dust in front of the roadheader while supplying fresh airflow to the driver and manned areas. Cheng *et al.*[41] developed a double-pressure double-extraction (DPDE) dust removal system and conducted parametric studies via numerical simulations to determine the optimal installation position of the air curtain generator. While those studies provide valuable insight on the effects of ventilation velocity, and different ventilation strategies on dust control in coal roadways, most of them only focused primarily on dust dispersion mechanisms within the heading face from the fixed dust source position.

Many researchers simplified the head-on face (i.e., the foremost working surface of a tunneling roadway during the excavation process, see Fig. 1) as the dust-generating surface. However, excavation operations are inherently dynamic, with the continuous movement of the cutting head causing the dust source position to shift over time. Jiang *et al.*[42] and Lu *et al.*[43] have recognized this issue, but their studies primarily focused on comparing the effects of nine critical dust source positions on dust diffusion, without considering the dynamic movement of the dust source. Moreover, most previous studies had concentrated on overall dust diffusion patterns within the roadway, paying limited attention to the dust distribution around workers and their particulate exposure risk.

To address the aforementioned gaps, in the present study, a full-scale heading face was numerically built to perform dust dispersion simulation. The dynamic dust dispersion pattern from the head-on face during the mining process was adopted using a user-defined function (UDF) and was further tracked using the Euler–Lagrangian model. The airflow patterns and dust trajectories are visualized, and the average residence time of particles with varying sizes is calculated and compared across various scenarios with different ventilation layouts and airflow rates. The further analysis focuses on the dust distribution around the driver of the roadheader, particularly within his respiratory zone. In addition, a backtracking analysis is performed on each particle entering the driver's respiratory zone to trace its origin. This study aims to investigate the dynamic dust dispersion pattern within the heading face and identify common characteristics of dust entering the driver's respiratory zone under different ventilation layouts.

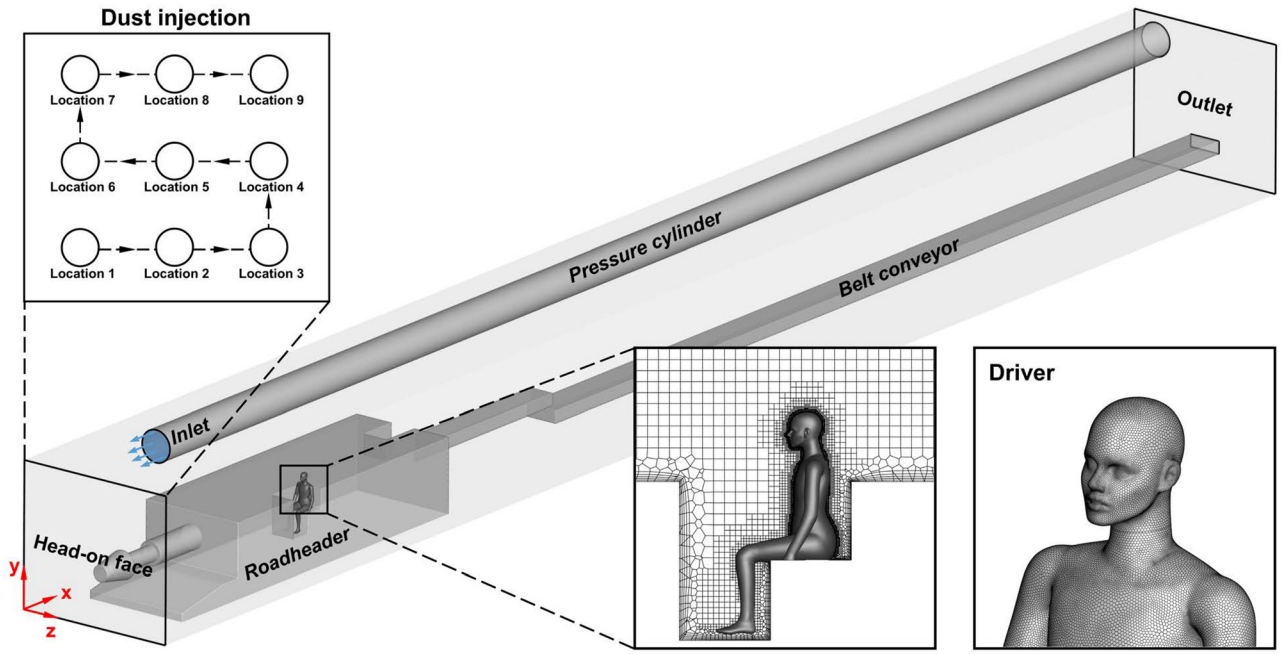

FIG. 1. The physical model and mesh details.

II. METHODOLOGY

A. The physical model and computational mesh

To study the dust transport behavior within the heading face, a typical excavation roadway of Shandong Energy Group was numerically built, as shown in Fig. 1. A simplified EBZ160 roadheader, with dimensions of $10 \times 2.6 \times 1.8\,m^3$ (length × height × width), was located at the front end of the roadway. The driver was positioned at the operator's position of the roadheader. The computational domain also included a pressure cylinder (a forced-air ventilation system commonly used in underground coal mines to supply fresh air to the heading face and remove dust from the working area) with a diameter of 0.8 m and a length of 36 m, suspended 2.9 m above the ground, along with a belt conveyor extending nearly the entire length of the roadway.

The previous study demonstrated that the placement of the ventilation cylinder significantly influences the airflow pattern within the heading face, thereby affecting dust transport behavior.[30] Consequently, the layout of the ventilation cylinder will directly impact the effectiveness of dust control. Implementing an appropriate ventilation layout is crucial for achieving efficient dust suppression. Building on this insight, the present study systematically investigated three different ventilation layouts, as illustrated in Fig. 2.

Computational meshes were generated using ANSYS Fluent Meshing. The entire computational domain was discretized by the poly-hexcore mesh to accommodate the complexity of the flow domains, particularly those involving intricate manikin geometry.[44] This meshing strategy involves filling the primary regions with hexahedral elements and switching to more adaptable polyhedral elements near complex geometrical boundaries for improved accuracy and flexibility (see Fig. 1). In comparison with the traditional unstructured tetrahedral mesh, the poly-hexcore mesh offers significant advantages by combining the strengths of polyhedral and hexahedral elements. It is more suitable for complex geometries, requiring fewer mesh elements while maintaining higher quality, facilitating improved computational convergence, and enabling greater accuracy.[45] To capture the flow pattern near the boundary layer, five near-wall prism layers were generated in this study.[46] Three sets of meshes with varying densities were utilized for the independence test, with total element counts of 2.21×10^6, 3.3×10^6, and 5.22×10^6. Velocity profiles along three lines, randomly selected from the computational domain, were extracted for comparison, as shown in Fig. 3. It can be observed that there was minimal deviation between the velocity profiles obtained from mesh 2 and mesh 3, demonstrating that the computed results would not significantly be affected by further mesh refinement. Therefore, the 3.3×10^6 mesh configuration was ultimately adopted for the subsequent calculations to balance the accuracy and computational cost.

B. Mathematical models

The dispersion of dust under the influence of airflow is classified as a gas–solid two-phase flow. In this study, the airflow was modeled as the continuous phase using the Eulerian approach, while dust particles were treated as the discrete phase and tracked individually by the Lagrangian method. To predict the airflow field within the roadway, the realizable k–epsilon model was employed as the turbulence model for the simulation. This model has been widely adopted in studies of roadway ventilation, and its superior accuracy and robust performance have been well-validated in previous research.[47–49] The transport equations for the turbulent kinetic energy (k) and dissipation rate (ε) in the realizable k–epsilon model can be expressed as[49,50]

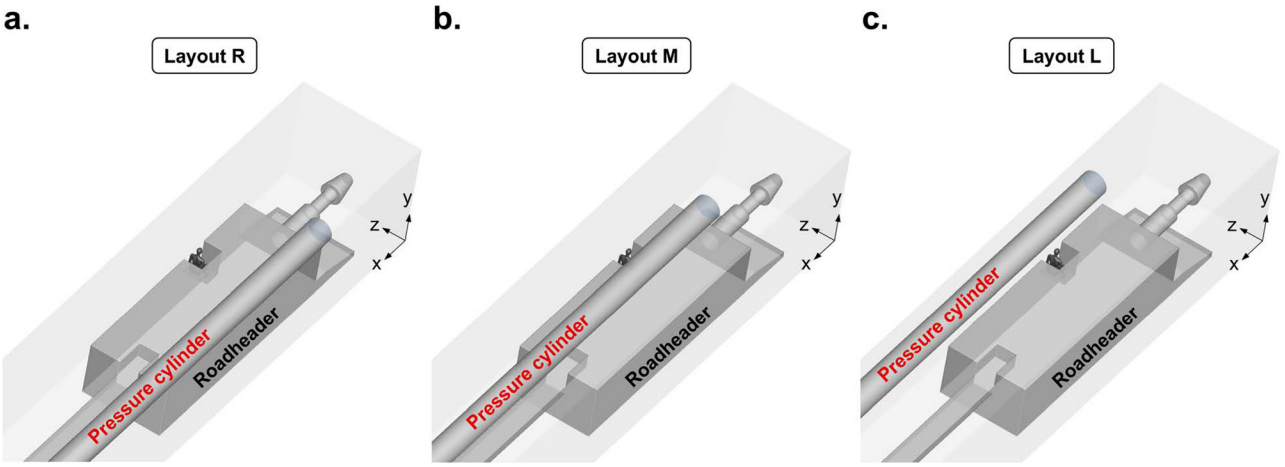

FIG. 2. Three layouts: (a) pressure cylinder on the right side, (b) pressure cylinder in the middle, and (c) pressure cylinder on the left side.

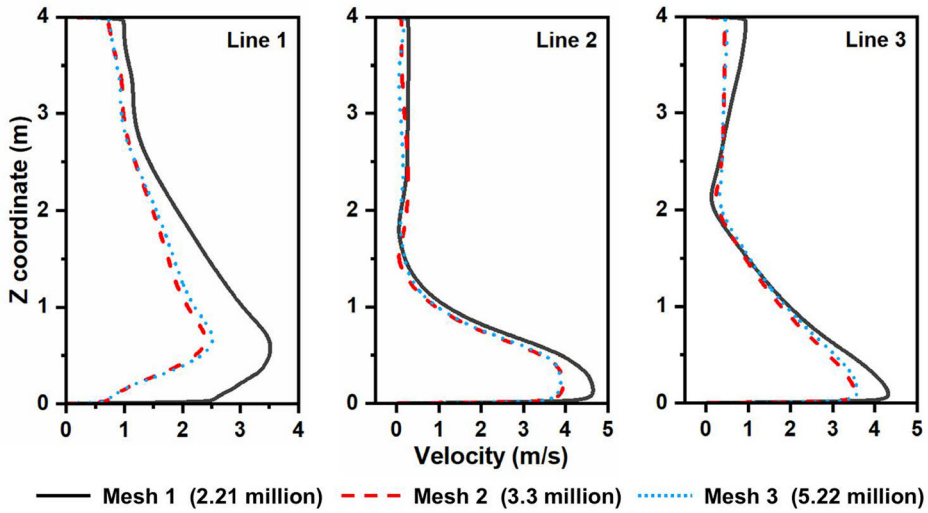

FIG. 3. Mesh independence test.

$$\frac{\partial}{\partial t}(\rho k)+\frac{\partial}{\partial x_j}(\rho k u_j)=\frac{\partial}{\partial x_j}\left[\left(\mu+\frac{\mu_t}{\sigma_k}\right)\frac{\partial k}{\partial x_j}\right]+G_k+G_b-\rho\varepsilon-Y_M+S_k, \tag{1}$$

$$\frac{\partial}{\partial t}(\rho\varepsilon)+\frac{\partial}{\partial x_j}(\rho\varepsilon u_j)=\frac{\partial}{\partial x_j}\left[\left(\mu+\frac{\mu_t}{\sigma_\varepsilon}\right)\frac{\partial \varepsilon}{\partial x_j}\right]+\rho C_1 S\varepsilon-\rho C_2\frac{\varepsilon^2}{k+\sqrt{v\varepsilon}}+C_{1\varepsilon}\frac{\varepsilon}{k}C_{3\varepsilon}G_b+S_\varepsilon, \tag{2}$$

$$C_1=\max\left[0.43,\frac{\eta}{\eta+5}\right], \tag{3}$$

$$\eta=S\frac{k}{\varepsilon}, \tag{4}$$

$$S=\sqrt{2S_{ij}S_{ij}}, \tag{5}$$

$$S_{ij}=\frac{1}{2}\left(\frac{\partial u_j}{\partial x_i}+\frac{\partial u_i}{\partial x_j}\right), \tag{6}$$

$$C_{3\varepsilon}=\tanh\left|\frac{v}{u}\right|, \tag{7}$$

$$C_{1\varepsilon}=1.44,\quad C_2=1.9,\quad \sigma_k=1.0,\quad \sigma_\varepsilon=1.2, \tag{8}$$

where t is the time, ρ is the fluid density, u is the fluid velocity, μ is the fluid dynamic viscosity, v is the fluid kinematic viscosity, μ_t is the eddy viscosity, G_k represents the generation of turbulence kinetic energy due to the mean velocity gradients, G_b is the generation of turbulence kinetic energy due to buoyancy, Y_M represents the contribution of the fluctuating dilatation in compressible turbulence to the overall dissipation rate, C_1 is used to correct the turbulent production term, C_2 is a correction coefficient associated with the turbulent dissipation term, $C_{1\varepsilon}$ and $C_{3\varepsilon}$ are correction factors related to buoyancy term, and σ_k, σ_ε are the turbulent Prandtl numbers for k and ε, respectively. S_k and S_ε

are user-defined source terms. S represents the magnitude of the mean strain rate tensor.

The turbulent viscosity is computed from[49,50]

$$\mu_t = \rho C_\mu \frac{k^2}{\varepsilon}, \tag{9}$$

$$C_\mu = \frac{1}{4.04 + \sqrt{6}\cos\varphi \frac{kU^*}{\varepsilon}}, \tag{10}$$

$$U^* \equiv \sqrt{S_{ij}S_{ij} + \widetilde{\Omega}_{ij}\widetilde{\Omega}_{ij}}, \tag{11}$$

$$\widetilde{\Omega}_{ij} = \overline{\Omega_{ij}} - 3\varepsilon_{ijk}\omega_k, \tag{12}$$

$$\varphi = \frac{1}{3}\cos^{-1}\left(\sqrt{6}\frac{S_{ij}S_{jk}S_{ki}}{\widetilde{S}^3}\right), \tag{13}$$

where C_μ is the coefficient for turbulent viscosity, φ is the angle parameter used in the realizable turbulence model, U^* denotes the characteristic velocity scale, S_{ij} is the strain rate tensor, and $\overline{\Omega_{ij}}$ is the mean rotation rate tensor observed in a moving reference frame with angular velocity ω_k.

For the discrete phase, to save computational cost, the dust particles were assumed to be solid spheres of varying sizes. Based on Newton's second law, the force balance equation for the particles used in this study can be expressed as follows:[47,51,52]

$$m_p \frac{d\vec{u}_p}{dt} = \vec{F}_B + \vec{F}_g + \vec{F}_D, \tag{14}$$

$$\vec{F}_B = -\frac{\pi}{6} d_p^3 \rho g, \tag{15}$$

$$\vec{F}_g = \frac{\pi}{6} d_p^3 \rho_p g, \tag{16}$$

$$\vec{F}_D = \frac{1}{8} C_D \rho \pi d_p^2 |\vec{u}_f - \vec{u}_p| (\vec{u}_f - \vec{u}_p), \tag{17}$$

$$C_D = a_1 + \frac{a_2}{Re} + \frac{a_3}{Re^2}, \tag{18}$$

$$Re \equiv \frac{\rho d_p |\vec{u}_p - \vec{u}_f|}{\mu}, \tag{19}$$

where ρ_p is the particle density, d_p is the particle diameter, g is the gravitational acceleration directed along the negative y-axis with a magnitude of 9.81 m/s^2, $\vec{F}_B$ is the buoyancy force, $\vec{F}_g$ is the gravitational force, $\vec{F}_D$ is the drag force, $\vec{u}_p$ and $\vec{u}_f$ are the particle and fluid velocities, respectively, C_D is the drag coefficient, Re is the Reynolds number for a spherical particle, and the coefficients a_1, a_2, a_3 are constant specified for different ranges of Re as provided by Morsi and Alexander.[53]

C. Numerical setup

This study utilized a numerical setup that reflects the actual working process. The face of the pressure cylinder was defined as the velocity inlet, while the exit of the roadway was set as the pressure outlet. To account for the dynamic changes in the dust source location caused by the movement of the roadheader's cutter plate during excavation, the dust source was positioned at the head-on face, and a Fluent user-defined function (UDF) was implemented to simulate the dust source moving in an S-shaped trajectory with a velocity of 0.05 m/s,[43] as illustrated in Fig. 1. The diameter distribution of the dust particles followed the Rosin-Rammler distribution, with the maximum, minimum, and mean diameter set to 100, 1.85, and 12 μm, respectively, based on our previous study.[54] In this study, 6000 particles were injected per second. These particles were released with an initial velocity corresponding to the local airflow velocity at the injection location, as determined by the continuous phase field. Steady-state airflow fields under two air supply velocities (i.e., 11 and 17 m/s) across three layouts were initially analyzed before tracking particulate contaminants.[55] To improve the robustness of the results, the second-order upwind discretization scheme was applied to momentum, turbulent kinetic energy, and dissipation rate. The pressure–velocity coupling was handled using the SIMPLE scheme. More detailed numerical calculation settings are shown in Table I.

To gain a deeper understanding of the effect of various pressure cylinder layouts and air supply velocities on dust transport within the heading face, six transient simulations were conducted. Numerical simulations were performed on a local Dell R7525 workstation. Utilizing 32 cores for parallel calculation, each simulation took approximately 48 h to complete, with a flow time duration of 300 s. In-house user-defined functions (UDFs) and Python codes were developed and employed for:

(1) injecting particles while moving in an S-shaped trajectory;
(2) calculating the average residence time of particles with various sizes;
(3) extracting the detailed information of particles entering the respiratory zone;

TABLE I. Numerical parameters summary.

Names	Type	Parameters	Names	Type	Parameters
General	Solver type	Pressure-based	Discrete phase	Particle material	Coal-hv
	Time	Transient		Diameter distribution	Rosin-Rammler
	Time step size	0.1 s		Total flow rate	0.006 kg/s
	Gravity	Y = −9.81 m/s^2		Min diameter	1.85 μm
Model	Viscous model	Realizable k–epsilon		Max diameter	100 μm
	Near-wall treatment	Standard wall functions		Mean diameter	12 μm
Boundary condition	Velocity inlet	11\17 m/s		Spread parameter	1.93
	Pressure outlet	Gauge pressure 0 Pa		Number of diameters	20

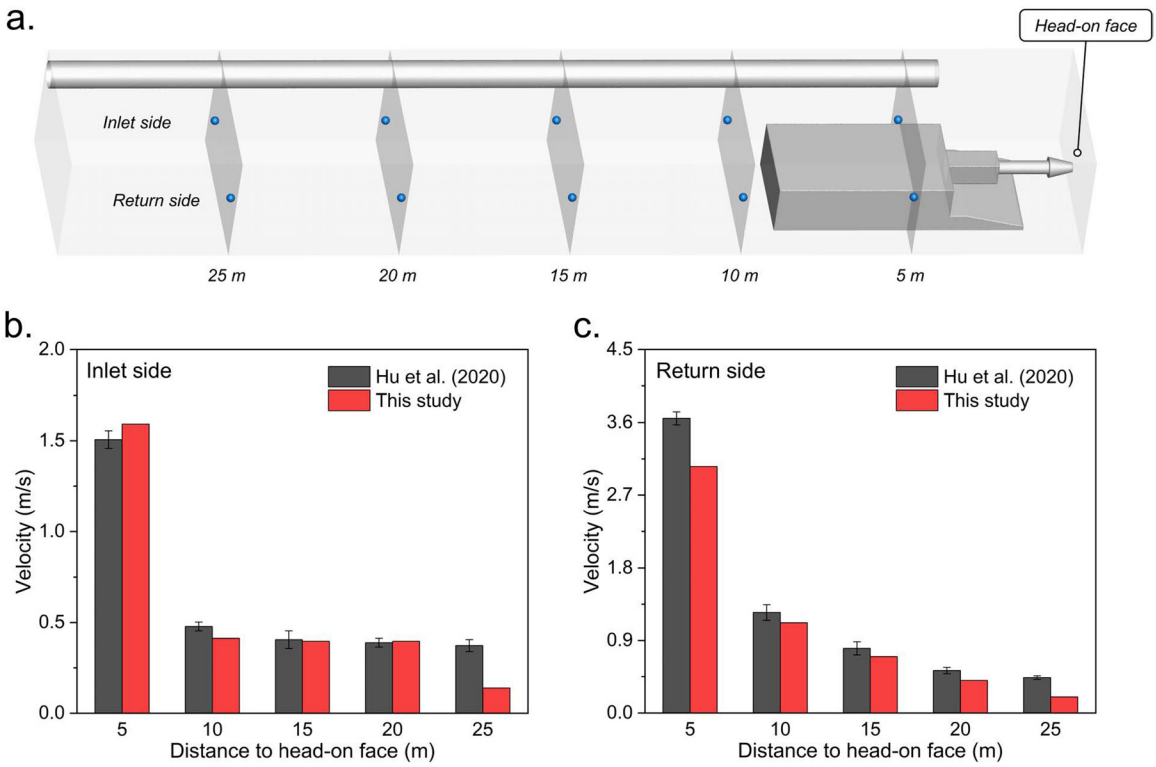

FIG. 4. The roadway modeling validation: (a) the physical model, (b) velocity profile comparison of the inlet side, and (c) velocity profile comparison of the return side.

(4) reverse tracking of the initial position of the particles;
(5) conducting particle size and source tracing analysis of particles entering the respiratory zone.

D. Model validation

The numerical results were validated by comparing the experimental data from Hu *et al.*[34] In their study, a $30 \times 5 \times 3.5\,m^3$ roadway was established, as shown in Fig. 4(a). Figures 4(b) and 4(c) present a comparison between experimental data and numerical results for both the inlet side (i.e., the side where fresh air enters the roadway, typically corresponding to the side where the pressure cylinder is installed) and return side (i.e., the side where dust-laden air exits, located opposite to the inlet side) at distances of 5, 10, 15, 20, and 25 m from the head-on face. The results reveal that the velocity profile within the heading face was accurately predicted. The numerical model successfully captured the decreasing trend in airflow velocity as the distance from the head-on face increased. It can be also observed that the deviation tended to grow with increasing distance from the head-on face. This discrepancy results from, on the one hand, the inherent limitations of the Reynolds-averaged Navier–Stokes (RANS) models, which rely on time-averaging the Navier–Stokes equations and therefore fail to capture transient flow behaviors. On the other hand, measurement errors must also be considered because airflow velocity is relatively low in these areas, and the complex and dynamic underground environment makes it difficult to obtain precise field data. Despite these challenges, both experimental data and numerical results successfully captured the significant reduction in airflow velocity at 10 m, followed by a gradual decline with increasing distance. The numerical model effectively reflected the overall airflow pattern within the heading face, demonstrating acceptable accuracy.

E. Definition of the human respiratory zone

As illustrated in Fig. 5, the respiratory zone was defined as a hemispherical region with a radius of 0.3 m, centered at the midpoint between the driver's mouth and nose.[56] Dust within the respiratory

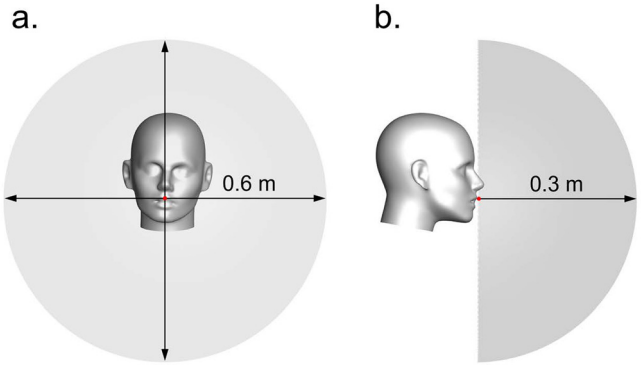

FIG. 5. Respiratory zone of the driver: (a) front view and (b) side view.

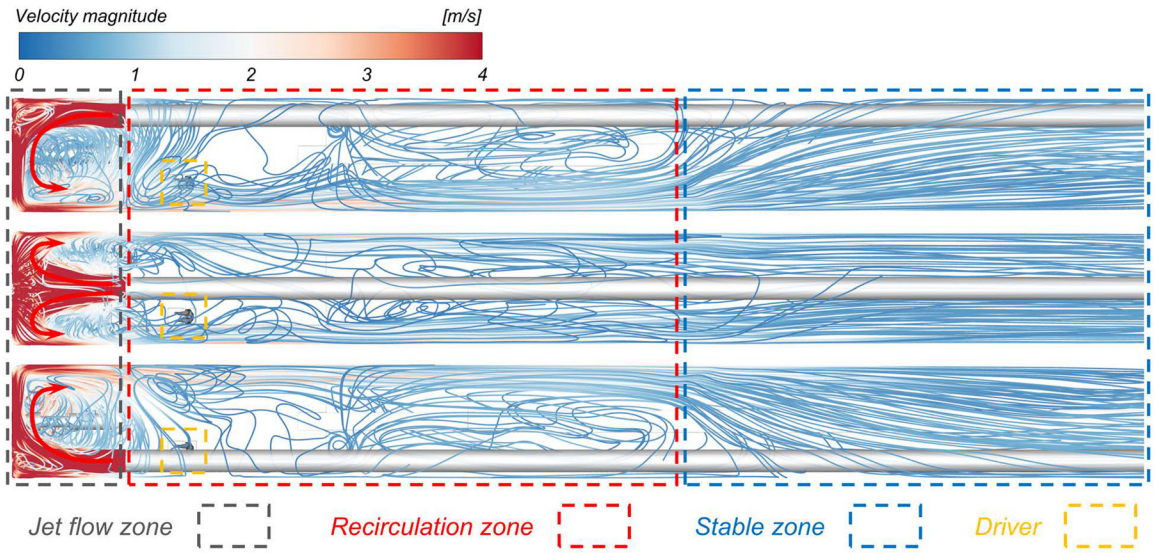

FIG. 6. Airflow streamlines for three layouts.

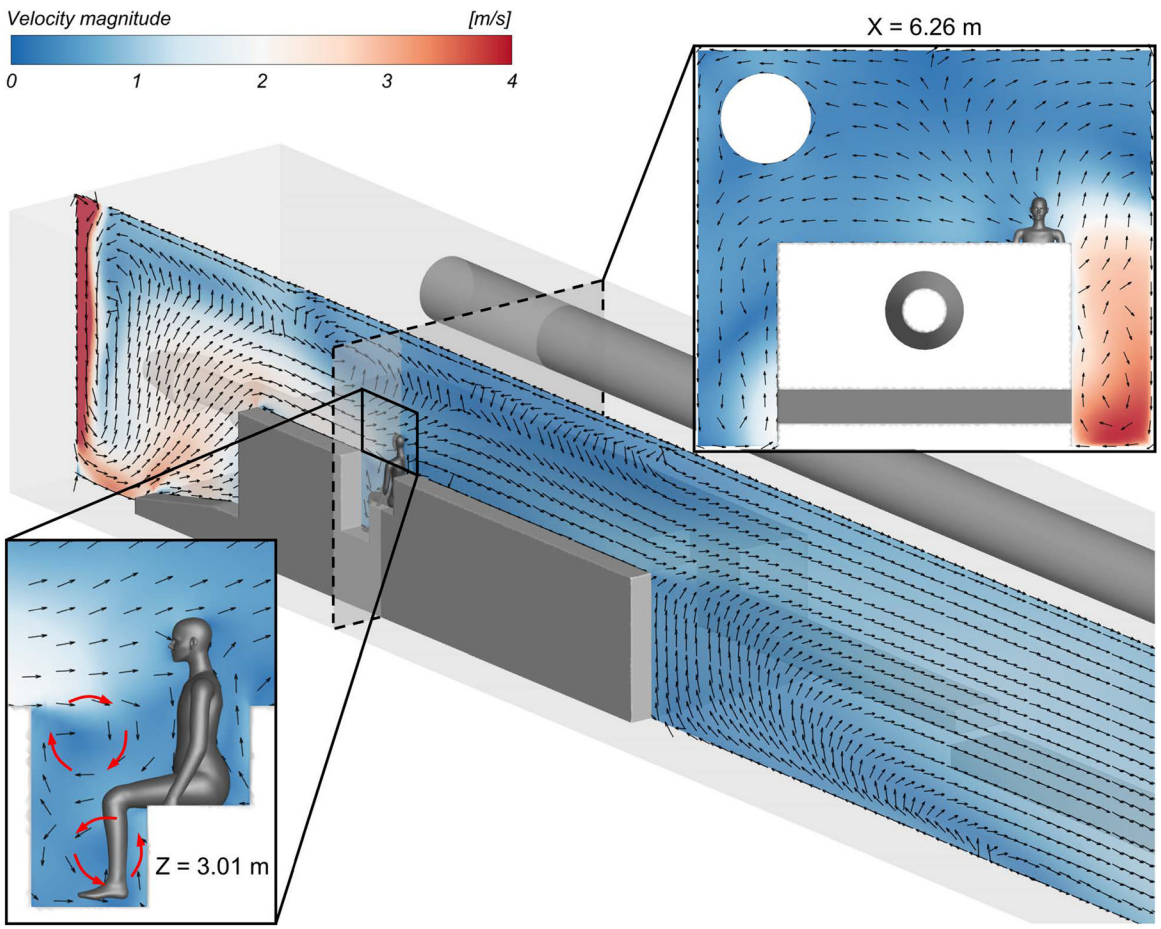

FIG. 7. Velocity fields in the driver's coronal (x = 6.26 m) and sagittal (z = 3.01 m) planes at a given air supply velocity of 11 m/s (layout R).

zone has a high potential to be inhaled, so conducting a detailed analysis of airborne particles in this zone is crucial for evaluating the risk of exposure to particulate contaminants for the driver.

III. RESULTS AND DISCUSSION

A. Airflow field and dust distribution

Figure 6 visualizes the airflow streamlines for three layouts. The airflow field could be distinctly divided into three zones: the jet flow zone, recirculation zone, and stable zone, consistent with findings from previous studies.[34,43] Due to the high-velocity airflow generated by the pressure cylinder, a ventilation-free jet was created within the first four meters of the roadway from the head-on face. Upon striking the head-on face, the airflow formed a wall jet. Constrained by the confined space, the airflow migrated laterally along the sidewall (when the pressure cylinder was arranged on the right, middle, or left side, the airflow would migrate laterally to the left, both sides or right side respectively, as indicated by the red arrows in Fig. 6) and flowed toward the end of the roadway. As the airflow moved to approximately 24 m from the head-on face, its velocity gradually decreased due to resistance along the roadway, eventually stabilizing. In all three layouts, the driver of the roadheader was located within the recirculation zone, where the airflow was more turbulent. This might increase the risk of driver being exposed to high dust concentrations.

Figure 7 provides the detailed velocity distribution in the driver's coronal and sagittal planes when the pressure cylinder was positioned on the right side. It can be observed that the high-velocity jet from the cylinder, after impacting the head-on face, moved toward the lower left corner of the roadway (i.e., the driver's side). This caused the formation of a distinct high-speed region in the lower-left corner of the roadway in the coronal plane (see the small figure in the upper-right corner of Fig. 7). From the sagittal perspective, the high-velocity jet rebounded after striking the head-on face. Induced by the ground and the surface of the roadheader, the airflow then moved toward the driver's face, which may potentially carry a significant amount of dust into the driver's respiratory zone. The airflow velocity near the driver decreased to approximately 0.5 m/s, with part of the airflow being obstructed by the driver's body, forming two recirculations around the upper body and legs. These recirculations might lead to substantial dust accumulation in these areas.

Figure 8 depicts the velocity distribution around the driver when the cylinder was in the middle. Similarly, the high-velocity jet generated

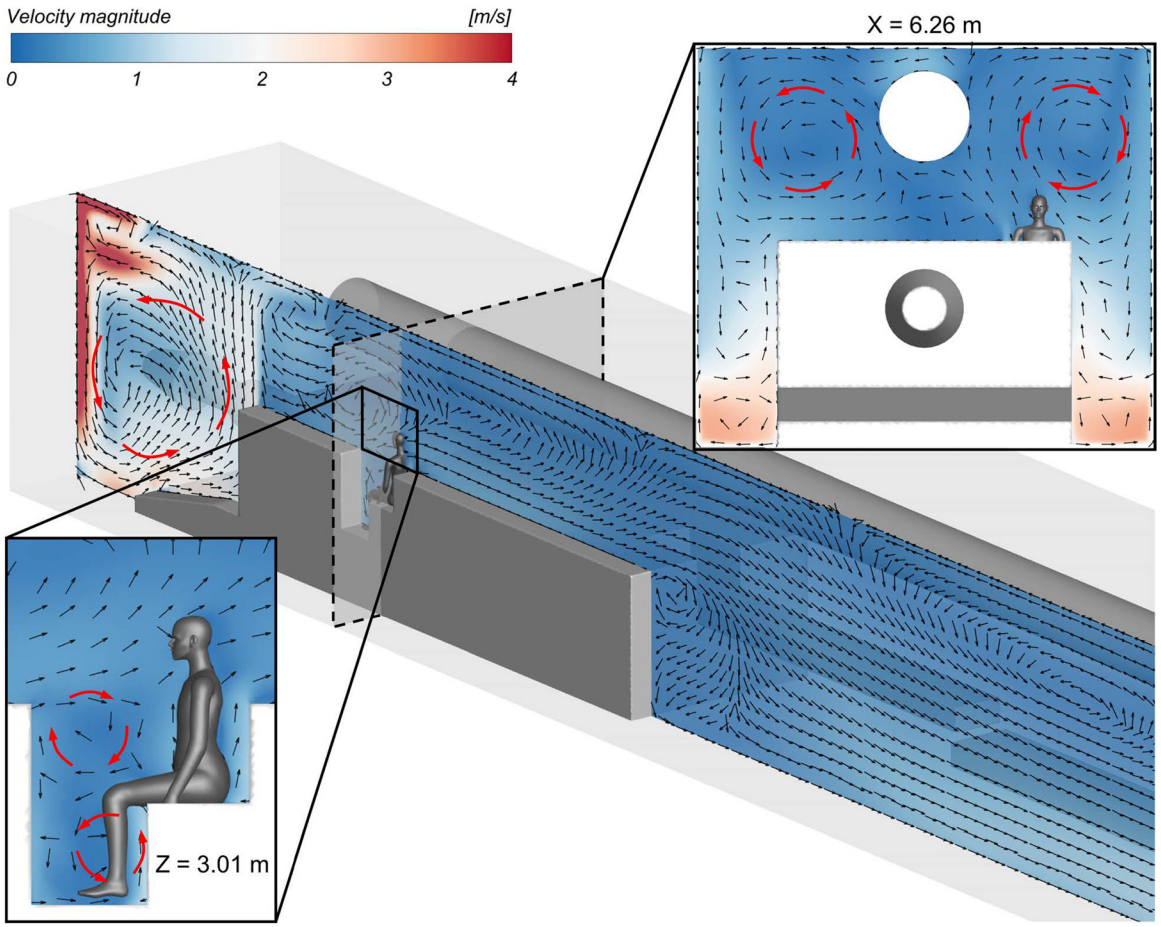

FIG. 8. Velocity fields in the driver's coronal (x = 6.26 m) and sagittal (z = 3.01 m) planes at a given air supply velocity of 11 m/s (layout M).

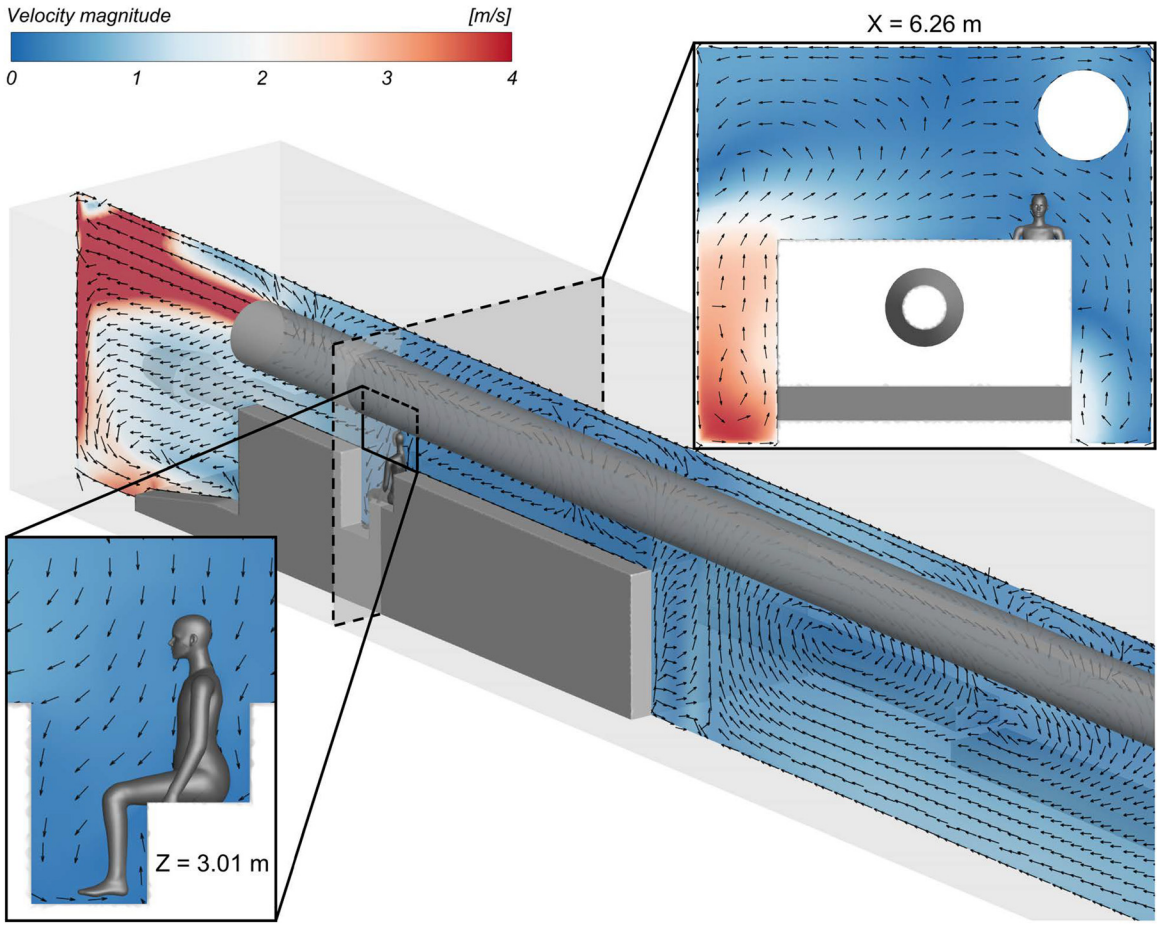

FIG. 9. Velocity fields in the driver's coronal (x = 6.26 m) and sagittal (z = 3.01 m) planes at a given air supply velocity of 11 m/s (layout L).

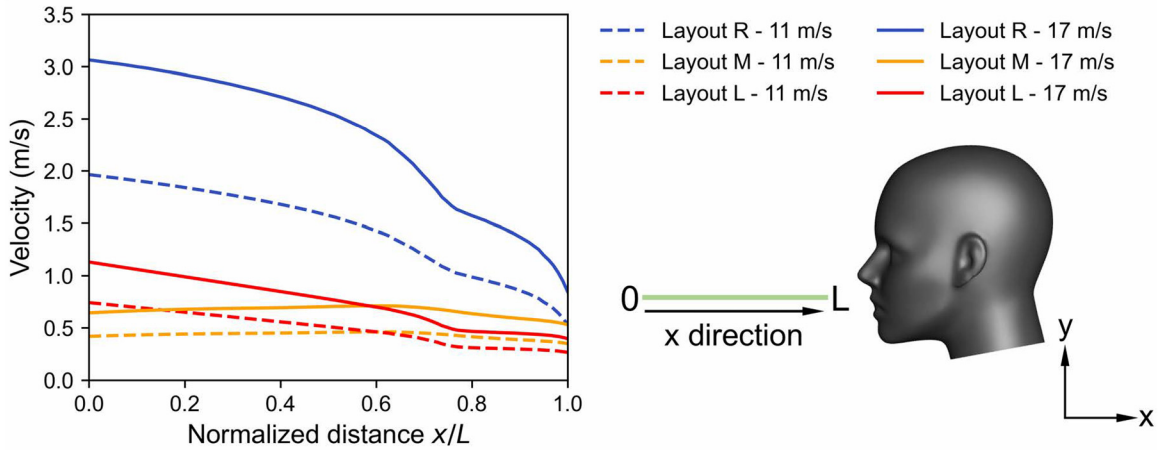

FIG. 10. Velocity profiles along a 1-m line in front of the driver's face under three ventilation layouts at air supply velocities of 11 and 17 m/s.

by the cylinder rebounded after impacting the head-on face and was further obstructed by the roadheader, resulting in a larger recirculation zone in front of the roadheader. The velocity distribution on the driver's coronal plane, shown in the upper-right corner of Fig. 8, revealed there were relatively higher velocity regions in the lower-left and lower-right corners of the roadway. Additionally, vortices with opposing directions were observed in the upper-left and upper-right corners, which might promote a more uniform dust distribution across the coronal plane. Compared to the cylinder positioned on the right side, the airflow velocity near the driver was much lower. However, the velocity vector patterns remained similar, with airflow directed toward the driver's face and the presence of two vortices near the upper body and legs.

The velocity distribution in the coronal and sagittal planes of the driver when the cylinder on the left side is shown in Fig. 9. In contrast to the configuration with the cylinder on the right side, the high-velocity jet hit the head-on face and was bounced back, moving toward the lower-right corner of the roadway. A higher velocity was observed near this lower-right corner of the roadway (see the upper-right subplot of Fig. 9). The airflow field in the vicinity of the driver had a lower velocity, and the airflow was blowing from the upper-right corner of the driver, differing from the first two layouts where the airflow was directed to the driver's face.

To carefully analyze the local environment around the driver, a 1-m line along the x-direction was extracted in front of the driver's face, and the velocity along this line was compared under different working conditions, as shown in Fig. 10. Overall, the velocity profile tended to decrease as it approached the driver's face. Among the various ventilation layouts, positioning the cylinder on the right side (i.e., layout R) had the most significant impact on the local airflow velocity, with the highest velocity observed along this line. When the air supply velocity was 17 m/s, the airflow velocity at the point closest to the driver's face could be up to 0.85 m/s. This can be attributed to the airflow characteristics of layout R, where the airflow moved toward the driver's face.

With the airflow field analyzed in detail, the dust transport characteristics within the heading face were further studied. Figure 11 demonstrates the spatial distribution of particles for the three layouts at an air supply velocity of 11 m/s with the same injection position. It can be clearly noticed that the dust dispersion was vastly affected by the local airflow pattern. In layout R and layout L, since the cylinder was arranged on one side of the roadway, the dust was transported with the airflow close to the other side of the wall toward the exit of the roadway. The dust appeared to be stratified, with larger particles having a tendency to settle and smaller particles spreading throughout the roadway. Similarly, when the dust injection position moved to the left half of the head-on face, the airflow carried the dust along the left wall toward the direction away from the head-on face in layout M. It was worth noting that the ability of the airflow to carry dust for

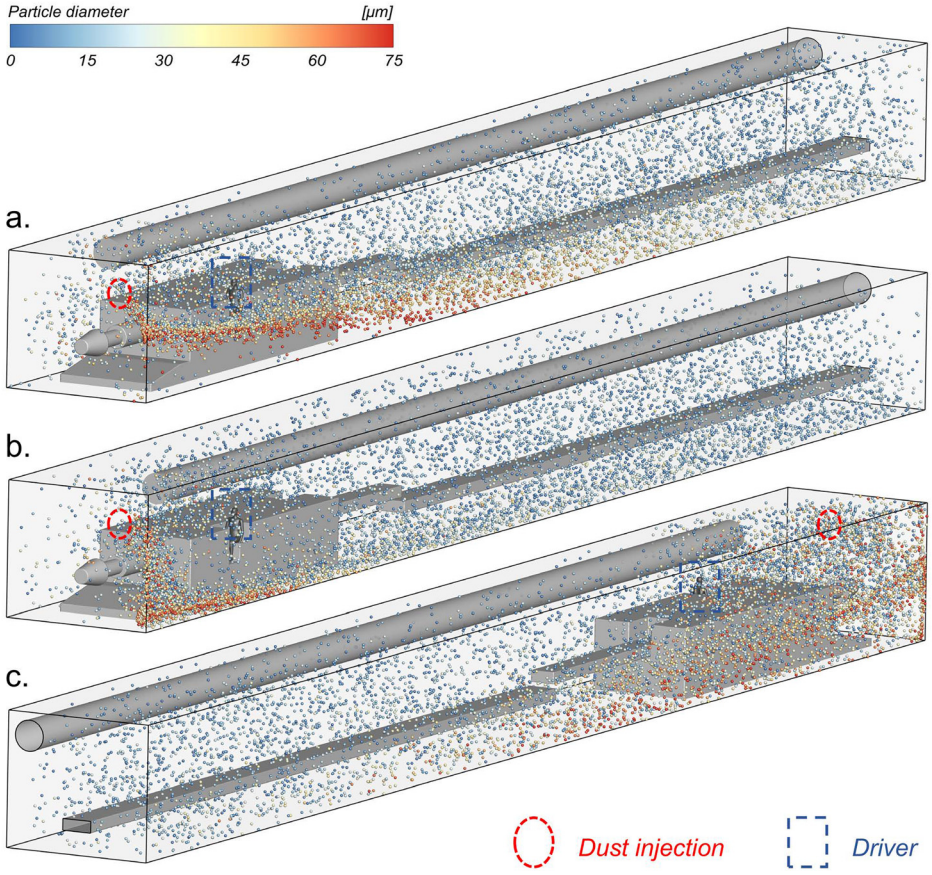

FIG. 11. Particle spatial distribution of the dust field for (a) layout R, (b) layout M, and (c) layout L.

transportation seemed to be weaker and dust with larger particle sizes was more easily deposited when the cylinder was arranged in the middle (i.e., layout M) compared to when the cylinder was arranged on one side of the roadway (i.e., layout R and layout L). Additionally, dust contaminants were dispersed to the side where the driver was located with the induce of the airflow in layout R. This inevitably resulted in a large amount of dust entering the driver's respiratory zone, posing a significant exposure risk. In contrast, when layout L was applied, the air flowed to the opposite side of the driver, reducing the dust reaching the driver's respiratory zone and thereby achieving a lower risk of exposure to dust contaminants.

Figure 12 presents the spatial distribution of particles when the dust injection position was aligned with the cylinder. In comparison with Fig. 11, there was no significant stratification of dust contaminants in Fig. 12. The dust was fully mixed and dispersed in front of the roadheader induced by the ventilation jet, without obvious deposition of larger particles, as seen in Figs. 12(a) and 12(c). However, in Fig. 12(b), when the cylinder was arranged in the middle of the roadway, the momentum of the ventilation jet dissipated rapidly toward both sides of the roadway. This reduced the carrying capacity of the airflow, causing larger particles to settle due to gravity, while smaller particles remained virtually unaffected and diffused throughout the roadway.

Figure 13 further investigates the impact of different layouts on dust transport characteristics by comparing the average residence time of dust particles with varying diameters within the heading face throughout the simulation period. Figure 13(a) depicts the average residence time of dust particles at an air supply velocity of 11 m/s. It can be found that as the particle diameter increased, the average residence time tended to decrease, with the magnitude of change becoming progressively smaller. Notably, the residence time was highly sensitive to the particle diameter of dust smaller than 25 μm. When the particle diameter increased to 40 μm, the residence time stabilized and showed minimal variation. This behavior could be attributed to the larger mass of bigger particles, where gravity became the dominant force, causing them to deposit on the ground more rapidly. In contrast, smaller particles were more influenced by airflow and remained suspended for longer durations. A further comparison of different layouts revealed a consistent general trend in residence time, and the difference was not significant between layout R and layout L. For dust particles smaller than 20 μm, the average residence time was significantly longer in layout M (i.e., 51.28 s) compared to layout R (i.e., 46.1 s) and layout L (i.e., 40.62 s), showing reductions of 10.1% and 20.79%, respectively. For particles larger than 40 μm, the shortest residence time was also observed in layout M (i.e., 9.47 s). When the cylinder was positioned centrally, the high-velocity jet struck the head-on face, generating two large recirculating flows in front of the roadheader. The dust interacted with the airflow, with smaller particles being continuously carried along, resulting in a longer residence time. In contrast, as

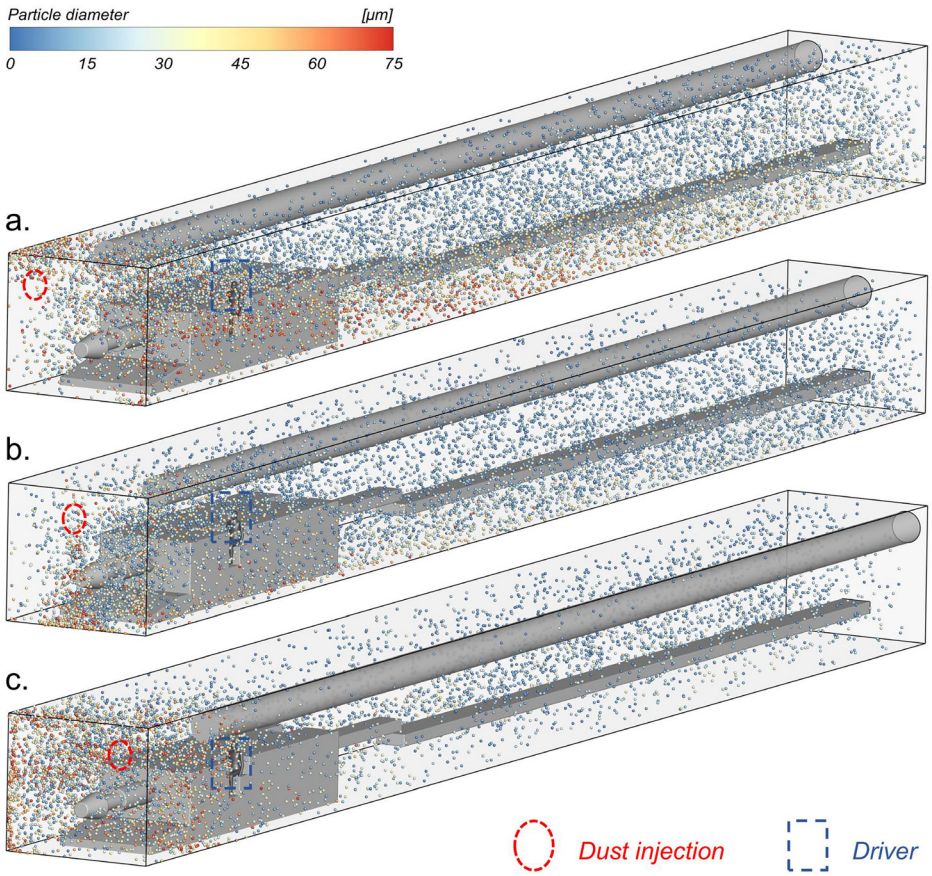

FIG. 12. Particle spatial distribution of the dust field for (a) layout R, (b) layout M, and (c) layout L when the dust injection position was aligned with the cylinder.

aforementioned, along with the weaker carrying capacity of the airflow, larger dust particles tended to settle on the ground more quickly, leading to a shorter residence time.

Figure 13(b) shows the average residence time of dust particles with varying sizes when the air supply velocity is 17 m/s. It is evident that the trend in the average residence time was similar to that observed in Fig. 13(a). However, the residence time of the dust was significantly reduced compared to the case with the air supply velocity of 11 m/s. For instance, the average residence times for particles smaller than 20 μm in layout R, layout M, and layout L were 34.9, 39.18, and 30.25 s respectively, representing reductions of 24.3%, 23.6%, and 25.53% compared to those at 11 m/s. The higher air supply velocity reduced the air exchange time within the roadway, resulting in more dust being discharged through the outlet by the airflow, rather than remaining in the roadway for the same duration, facilitating the removal of most dust and improvement of the overall environment in the roadway.

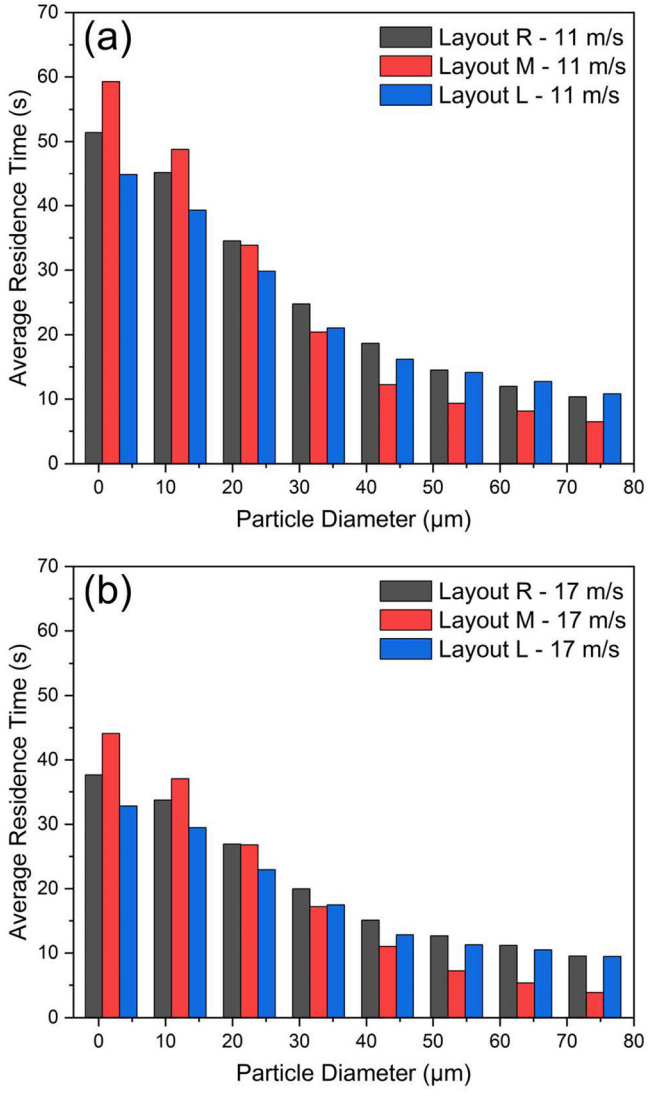

FIG. 13. Dust average residence time with various layouts: (a) $V_{supply} = 11$ m/s and (b) $V_{supply} = 17$ m/s.

B. Dust distribution in the driver's local environment

To further investigate the particulate exposure of the driver within the heading face, detailed data on the particles entering the respiratory zone were extracted. The total number of particles entering the respiratory zone during the entire simulation was calculated, normalized, and compared across six different scenarios (see Fig. 14). It can be clearly observed that layout R resulted in a higher number of particles entering the driver's respiratory zone, while the number of particles entering the respiratory zone was similar with layout M and layout L. Specifically, layout R increased the number of particles entering the respiratory zone by approximately 202.72% compared to layout M and 186.75% compared to layout L. Furthermore, increasing the air supply velocity did not significantly affect the number of particles entering the respiratory zone. This suggested that adopting a reasonable cylinder layout might be more effective in reducing the driver's exposure to particulate contaminants than simply increasing the fresh air flow rate.

Figure 15 compares the particle size distributions of dust entering the driver's respiratory zone throughout the simulation process across six different cases. It is evident that the particle size distributions entering the respiratory zone were similar for layouts with the same configuration. Specifically, smaller respirable dust (i.e., $d_p < 7.07$ μm) was more likely to enter the driver's respiratory zone, while the proportion of larger particles decreased as their size increased. Among the various layouts, layout R exhibited the highest proportion of particles larger than 60 μm. This was due to the airflow being directed toward the driver, allowing even larger particles to overcome inertia and follow the airflow into the respiratory zone. Moreover, when adopting layout M, the weaker carrying capacity of the airflow resulted in a significant reduction in the proportion of larger particles (i.e., $d_p > 40$ μm) entering the respiratory zone, and the proportion of respirable dust was highest. This suggested that positioning the cylinder in the middle may

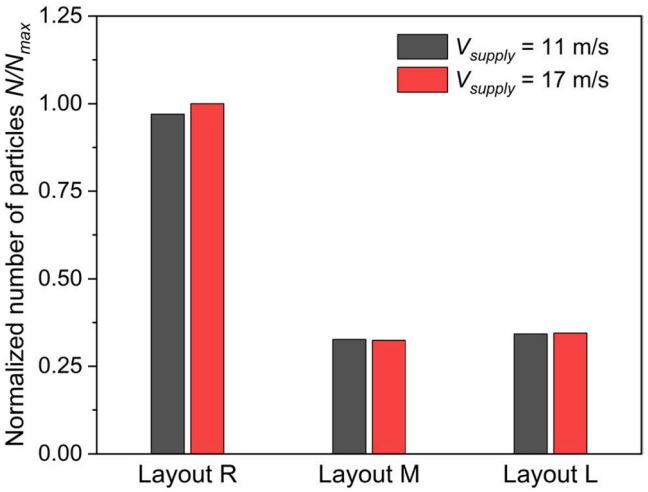

FIG. 14. Normalized number of particles entering the driver's respiratory zone.

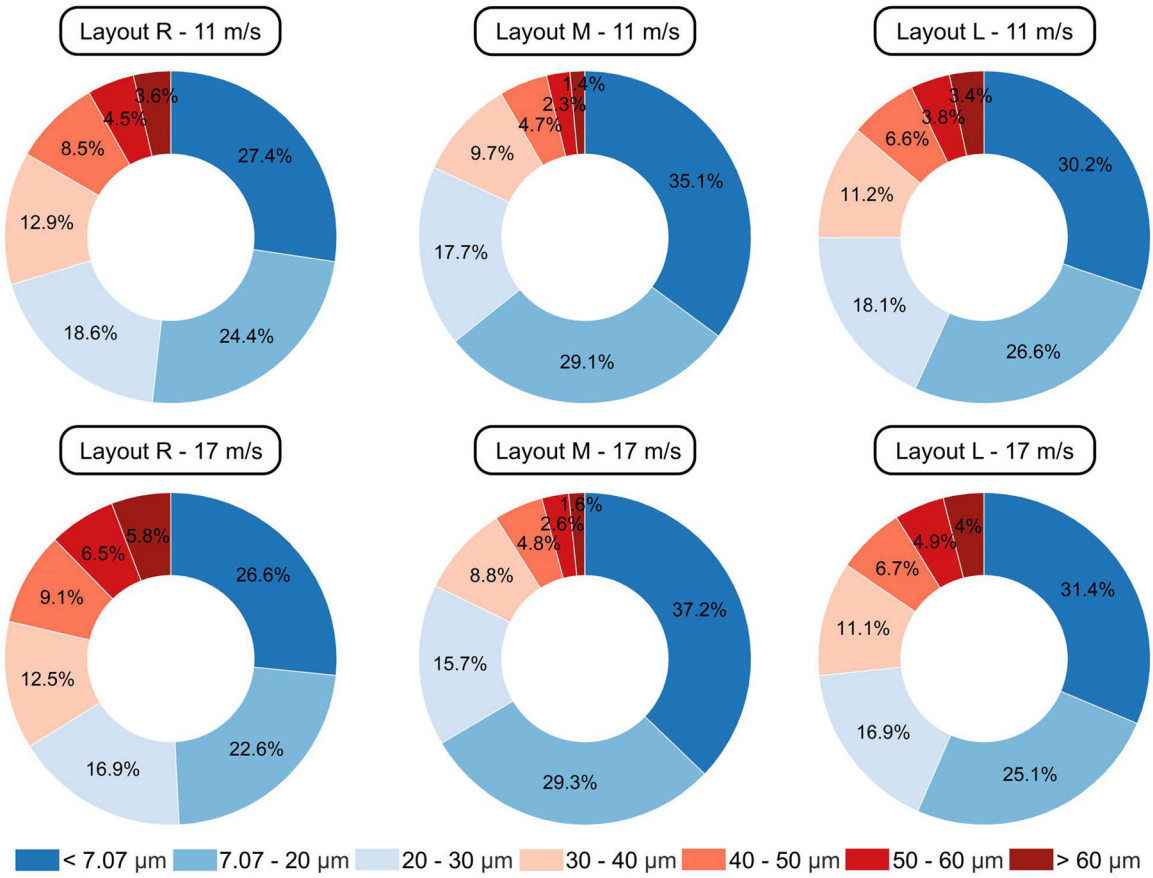

FIG. 15. Particle size distribution of dust entering the driver's respiratory zone.

not be optimal, as it increases the risk of the driver inhaling respirable dust. Overall, layout L appeared to present the driver with a relatively low risk of particulate exposure compared to the other configurations.

To understand the dynamic characteristics of dust entering the driver's respiratory zone across multiple layouts, a source-tracking analysis was performed on all particles entering the respiratory zone during the entire simulation. Each particle was reverse-traced to determine its initial release position, and the dust injection area on the head-on face was divided into $0.5 \times 0.5\,m^2$ grids. The proportion of particles originating from each grid cell was calculated based on their initial positions, as shown in Fig. 16. The particle source patterns were similar for the same layout, and the air supply velocity didn't significantly affect the source pattern of particles. In layout R, the majority of particles entering the driver's respiratory zone originated from the upper-left corner of the dust injection surface, with relatively fewer particles from the lower half of the surface reaching the respiratory zone. For layout M, most particles entering the respiratory zone originated from the left half of the dust injection surface, primarily due to the driver being positioned on the left side of the roadway. In layout L, dust particles from the upper-right corner of the dust injection surface were more likely to enter the driver's respiratory hemisphere. In all, it can be found that dust from the upper part of the dust injection surface was more likely to enter the driver's respiratory zone across all layouts. The existing airflow pattern would suspend the particle to the lower level, thereby increasing the likelihood of particles reaching the respiratory zone.

IV. LIMITATIONS

This study developed a full-scale heading face model to investigate the effects of different ventilation layouts on dust dispersion and driver's particulate exposure, while several limitations should be acknowledged.

This study primarily employs the RANS model. Due to the inherent limitations of RANS, it cannot capture instantaneous and intense turbulent fluctuations. In particular, the ventilation jet flow zone is characterized by strong unsteadiness and intermittency, which RANS may inadequately resolve, potentially affecting the accuracy of particle transport predictions. Future research could consider higher-fidelity models, such as large eddy simulation (LES), to better capture these complex turbulent structures.

Moreover, due to the significant local fluctuations in the airflow field within the heading face, the Saffman lift force induced by strong shear and the Basset history force resulting from rapid variations in fluid velocity may affect local particle dispersion. In this study, the particle motion model primarily considers drag, buoyancy, and gravitational forces, consistent with modeling approaches commonly adopted

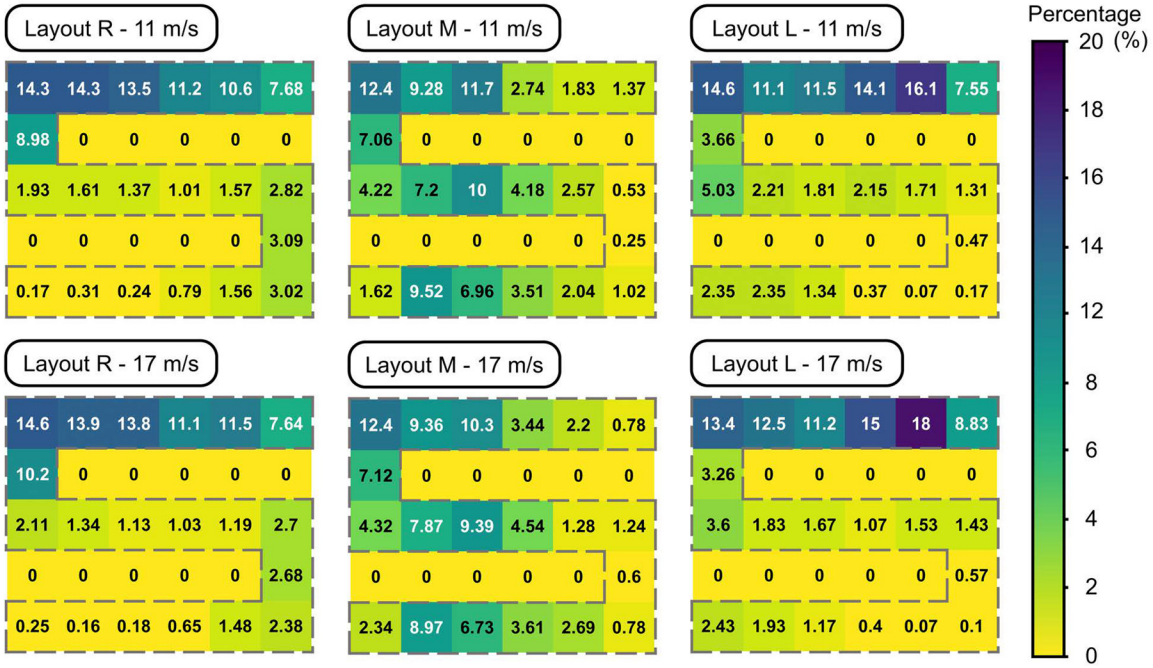

FIG. 16. Source tracking of dust entering the driver's respiratory zone.

in related research.[40,41,43,49] To better capture the particle dynamics in complex flow regions, future work could incorporate additional forces such as the Saffman lift and Basset history forces, particularly in areas characterized by intense shear or rapid velocity fluctuations.

V. CONCLUSION

In this study, a full-scale heading face was numerically modeled to assess the dust exposure risk to the driver under three different ventilation layouts, i.e., layout R (pressure cylinder on the right side), layout M (pressure cylinder in the middle), and layout L (pressure cylinder on the left side). The dynamic dust dispersion pattern from the head-on face during the mining process was implemented using a user-defined function (UDF) and further tracked using the Euler–Lagrangian model. Detailed airflow patterns and dust transport characteristics within the heading face and the driver's local environment were thoroughly evaluated, with a particular focus on the driver's respiratory zone. The major findings of this study were summarized as follows:

(1) When forced ventilation was applied, the airflow field within the heading face could be divided into three regions: the jet flow zone, the recirculation zone, and the stable zone. In all three layouts, it was found that the driver was located in the turbulent recirculation zone. Under layout R and layout M, two vortex areas were observed around the driver's upper body and legs, where dust particles were more likely to accumulate, increasing the risk of particulate matter inhalation.
(2) The average residence time was highly sensitive to dust particles with diameters smaller than 25 μm, while particles larger than 40 μm were more likely to be deposited on the ground rapidly. For layout M, with a total suspension time of 300 s and an air supply velocity of 11 m/s, particles with a diameter less than 20 μm exhibited the longest average residence time (i.e., 51.28 s), which was 11.24% and 26.24% longer than the residence time in layout R and layout L. Therefore, layout R and layout L, i.e., the cylinder was on the right and left side, are expected to be more effective in improving the overall working environment within the heading face compared to layout M.
(3) Among all layouts, the source-tracking analysis revealed that particles from the upper part of the dust injection surface were more likely to enter the driver's respiratory zone. The number of particles entering the respiratory zone was highest in layout R, being approximately 202.72% greater than in layout M and 186.75% greater than in layout L. The largest proportion of particles entering the respiratory zone was respiratory dust with small particle sizes (i.e., $d_p < 7.07$ μm). Additionally, it was found that raising the air supply velocity had minimal impact on the number of particles entering the respiratory zone, indicating that merely increasing the fresh air supply rate was insufficient to reduce the driver's particulate exposure risk.
(4) Compared to layout M, layout R, and layout L could inhibit the suspension of small particles to some extent, which was more conducive to improving the overall environment within the heading face. However, with layout L, the driver's exposure risk was reduced by approximately 65.12% compared to layout R. Positioning the pressure cylinder on the same side as the driver (i.e., layout L) was found to be the relatively optimal configuration.

ACKNOWLEDGMENTS

This work was funded by the National Key Research and Development Program of China (No. 2024YFC3015003), the National

Natural Science Foundation of China (Grant No. 52174222), and the Basic Research Program of Xuzhou (No. KC23050).

AUTHOR DECLARATIONS

Conflict of Interest

The authors have no conflicts to disclose.

Author Contributions

Jiaqi Fan: Conceptualization (equal); Investigation (equal); Methodology (equal); Software (equal); Visualization (equal); Writing – original draft (equal); Writing – review & editing (equal). **Xueren Li:** Conceptualization (equal); Investigation (equal); Methodology (equal); Supervision (equal); Writing – original draft (equal); Writing – review & editing (equal). **Ruipeng Xu:** Data curation (equal); Investigation (equal). **Zhaoxing Li:** Formal analysis (equal); Software (equal). **Changgeng Gui:** Software (equal); Validation (equal). **Shihang Li:** Conceptualization (equal); Investigation (equal); Supervision (equal); Writing – original draft (equal). **Zhengbiao Peng:** Conceptualization (equal); Investigation (equal); Supervision (equal); Writing – original draft (equal). **Fan Geng:** Conceptualization (equal); Funding acquisition (equal); Project administration (equal); Resources (equal); Supervision (equal); Writing – original draft (equal); Writing – review & editing (equal). **Xinjian He:** Funding acquisition (equal); Project administration (equal); Resources (equal); Supervision (equal); Writing – review & editing (equal).

DATA AVAILABILITY

The data that support the findings of this study are available from the corresponding authors upon reasonable request.

REFERENCES

[1]X. Tian, C. An, and Z. Chen, "The role of clean energy in achieving decarbonization of electricity generation, transportation, and heating sectors by 2050: A meta-analysis review," Renewable Sustainable Energy Rev. **182**, 113404 (2023).
[2]Ministry of Natural Resources PRC, see https://m.mnr.gov.cn/sj/sjfw/kc_19263/zgkczybg/202410/t20241022_2871217.html for "China mineral resources" (2024).
[3]W. Nie, Q. Tian, W. Niu, Q. Bao, M. Yuan, W. Zhou, F. Yu, and X. Yan, "Carboxymethyl cellulose sodium gel: A modified material used to suppress coal dust pollution," Environ. Res. **215**, 114234 (2022).
[4]China Energy News, see https://paper.people.com.cn/zgnyb/html/2023-05/22/content_25990044.htm for "Urgent need to accelerate the shift in intelligent coal mining in China" (2023).
[5]M. Guo, Y. Qin, H. Hou, F. Zhang, F. Tang, and H. Xu, "Prediction of airflow temperature in underground long-distance excavation roadway and ventilation duct: Numerical simulation and field test validation," Therm. Sci. Eng. Prog. **46**, 102247 (2023).
[6]J. Li, L. Wu, and H. Chen, "Analysis of thermal comfort and threshold range of airflow supply parameters for different types of work in humid-heat coal mines," Case Stud. Therm. Eng. **44**, 102826 (2023).
[7]H. Qiaoyun, Z. Yi, L. Kongqing, and Z. Shenghua, "Computational evaluation of cooling system under deep hot and humid coal mine in China: A thermal comfort study," Tunnelling Underground Space Technol. **90**, 394–403 (2019).
[8]Y. Wang, Y. Wang, X. Wang, C. Wang, and G. Li, "Experimental investigation on physiological and perceptual thermal responses through simulated hot-humid deep mine conditions," Build. Environ. **255**, 111435 (2024).
[9]Y. Liu, J. Li, Y. Wang, G. Li, Z. Hu, H. Chen, and K. Zhou, "Comparison of artificial refrigeration cooling schemes for high temperature tunneling roadway in deep mines—The case of Yunnan Dahongshan Copper Mine," Case Stud. Therm. Eng. **61**, 104997 (2024).
[10]D. Yang, K. Peng, Y. Zheng, Y. Chen, J. Zheng, M. Wang, and S. Chen, "Study on the characteristics of coal and gas outburst hazard under the influence of high formation temperature in deep mines," Energy **268**, 126645 (2023).
[11]A. M. Donoghue, M. J. Sinclair, and G. P. Bates, "Heat exhaustion in a deep underground metalliferous mine," Occup. Environ. Med. **57**(3), 165–174 (2000).
[12]N. Qin, H. Yu, J. Zhao, Y. Xie, and X. Li, "Numerical simulation of multi-factor influence mechanism in 'barrier closure' dust removal technology," J. Build. Eng. **97**, 110730 (2024).
[13]C. Guo, W. Nie, C. Xu, H. Peng, C. Zhang, S. Li, N. Yue, Z. Liu, S. Yang, Q. Ma, and M. Li, "A study of the spray atomization and suppression of tunnel dust pollution based on a CFD-based simulation," J. Cleaner Prod. **276**, 123632 (2020).
[14]L. Yuan, "Scientific conception of coal mine dust control and occupational safety," J. China Coal Soc. **45**(1), 1–7 (2020).
[15]H. Zhang, W. Han, Y. Xu, and Z. Wang, "Analysis on the development status of coal mine dust disaster prevention technology in China," J. Healthcare Eng. **2021**(1), 1.
[16]Y. Zheng, C. Feng, G. Jing, X. Qian, X. Li, Z. Liu, and P. Huang, "A statistical analysis of coal mine accidents caused by coal dust explosions in China," J. Loss Prev. Process Ind. **22**(4), 528–532 (2009).
[17]R. Gao, P. Wang, Y. Li, and R. Liu, "Determination of optimal blowing-to-suction flow ratio in mechanized excavation face with wall-mounted swirling ventilation using numerical simulations," Int. J. Coal Sci. Technol. **8**(2), 248–264 (2021).
[18]K. A. Wallace and W. M. Cheung, "Development of a compact excavator mounted dust suppression system," J. Cleaner Prod. **54**, 344–352 (2013).
[19]V. Castranova and V. Vallyathan, "Silicosis and coal workers' pneumoconiosis," Environ. Health Perspect. **108**(suppl 4), 675–684 (2000).
[20]R. A. Pinho, F. Bonatto, M. Andrades, M. L. C. Frota, C. Ritter, F. Klamt, F. Dal-Pizzol, J. M. Uldrich-Kulczynski, and J. C. F. Moreira, "Lung oxidative response after acute coal dust exposure," Environ. Res. **96**(3), 290–297 (2004).
[21]T. Liu and S. Liu, "The impacts of coal dust on miners' health: A review," Environ. Res. **190**, 109849 (2020).
[22]G. Zhou, Y. Liu, B. Sun, Z. Liu, C. Xu, R. Liu, Q. Zhang, and Y. Wang, "Study on the fine particles deposition law in the bronchus of miners affected by dust pollution in the anchor excavation working environment," J. Mol. Liq. **393**, 123620 (2024).
[23]National Health Commission PRC, see http://www.nhc.gov.cn/xcs/s3574/202204/2fbf355668df4fd0ade8b5c3cf455f95.shtml for "Transcript of the April 25, 2022 press conference by the NHC of the PRC" (2022).
[24]H. Wang, Q. Ye, Y. Chen, and T. Li, "Epidemiology of coal miners' pneumoconiosis and its social determinants: An ecological study from 1949 to 2021 in China," Chin. Med. J. Pulm. Crit. Care Med. **1**(1), 46–55 (2023).
[25]C. Xu, W. Wang, K. Wang, M. Wang, Y. Hu, L. Guo, T. Yang, and Y. Yuan, "Dust transport law and ventilation parameters optimization in heading face under long-pressure and short-pumping ventilation conditions," Phys. Fluids **37**(2), 023377 (2025).
[26]A. R. Kumar, S. Schafrik, and T. Novak, "Multi-phase computer modeling and laboratory study of dust capture by an inertial Vortecone scrubber," Int. J. Min. Sci. Technol. **30**(3), 287–291 (2020).
[27]G. Zhang, G. Zhou, S. Song, L. Zhang, and B. Sun, "CFD investigation on dust dispersion pollution of down/upwind coal cutting and relevant countermeasures for spraying dustfall in fully mechanized mining face," Adv. Powder Technol. **31**(8), 3177–3190 (2020).
[28]J. Zhu, X. He, L. Wang, X. Liao, G. Teng, and P. Jing, "Performance of N95 elastomeric respirators in high humidity and high coal dust concentration environment," Int. J. Min. Sci. Technol. **32**(1), 215–224 (2022).
[29]J. Colinet, C. N. Halldin, and J. Schall, *Best Practices for Dust Control in Coal Mining: Second Edition* (The National Institute for Occupational Safety and Health (NIOSH), Pittsburgh, PA, 2021).
[30]W. Nie, W. Wei, X. Ma, Y. Liu, H. Peng, and Q. Liu, "The effects of ventilation parameters on the migration behaviors of head-on dusts in the heading face," Tunnelling Underground Space Technol. **70**, 400–408 (2017).
[31]W. Nie, W. Wei, P. Cai, Z. Liu, Q. Liu, H. Ma, and H. Liu, "Simulation experiments on the controllability of dust diffusion by means of multi-radial vortex airflow," Adv. Powder Technol. **29**(3), 835–847 (2018).
[32]W. Ren, J. Shi, J. Zhu, and Q. Guo, "An innovative dust suppression device used in underground tunneling," Tunnelling Underground Space Technol. **99**, 103337 (2020).

[33]H. Zheng, B. Jiang, Y. Zheng, Y. Zhao, and H. Wang, "Experimental study on forced ventilation and dust-control in a heading face based on response surface method," Process Saf. Environ. Prot. **175**, 753–763 (2023).
[34]S. Hu, Q. Liao, G. Feng, Y. Huang, H. Shao, Y. Gao, and F. Hu, "Influences of ventilation velocity on dust dispersion in coal roadways," Powder Technol. **360**, 683–694 (2020).
[35]F. Geng, G. Luo, F. Zhou, P. Zhao, L. Ma, H. Chai, and T. Zhang, "Numerical investigation of dust dispersion in a coal roadway with hybrid ventilation system," Powder Technol. **313**, 260–271 (2017).
[36]F. Geng, C. Gui, H. Teng, J. Tang, H. Niu, F. Zhou, C. Liu, S. Hu, and S. Li, "Dispersion characteristics of dust pollutant in a typical coal roadway under an auxiliary ventilation system," J. Cleaner Prod. **275**, 122889 (2020).
[37]Z. Wang, S. Li, T. Ren, J. Wu, H. Lin, and H. Shuang, "Respirable dust pollution characteristics within an underground heading face driven with continuous miner—A CFD modelling approach," J. Cleaner Prod. **217**, 267–283 (2019).
[38]C. Hou, H. Yu, X. Yang, W. Cheng, Y. Wang, and Y. Ye, "Research on dust removal technology of large eddy dust collecting and swirl airflow distribution in the fully-mechanized excavation face," Powder Technol. **411**, 117922 (2022).
[39]C. Hou, H. Yu, Y. Ye, X. Yang, Y. Wang, and W. Cheng, "Study on dust pollution characteristics and optimal dust control parameters during tunnel excavation by CFD simulation," Adv. Powder Technol. **34**(11), 104217 (2023).
[40]N. Qin, H. Yu, P. Wang, X. Li, X. Qiao, and W. Cheng, "Study on multiple influence mechanism of airflow-dust-gas coupling diffusion under large vortex flow technology," Build. Environ. **257**, 111538 (2024).
[41]C. Cheng, Q. Liu, Y. Hua, L. Guo, H. Zhang, Z. Zhu, and W. Nie, "Analysis of a double-pressure double-extraction (DPDE) control dust removal system and optimal installation position of an air curtain generator," Energy **313**, 134022 (2024).
[42]W. Jiang, X. Xu, Z. Wen, and L. Wei, "Applying the similarity theory to model dust dispersion during coal-mine tunneling," Process Saf. Environ. Prot. **148**, 415–427 (2021).
[43]X. Lu, C. Shen, Y. Xing, H. Zhang, C. Wang, G. Shi, and M. Wang, "The spatial diffusion rule and pollution region of disorganized dust in the excavation roadway at different roadheader cutting positions," Powder Technol. **396**, 167–180 (2022).
[44]X. Li, Y. Yan, X. Fang, F. He, and J. Tu, "Towards understanding of inhalation exposure of pilots in the control cabin environment," Build. Environ. **242**, 110572 (2023).
[45]X. Li, Z. Chen, Y. Tang, Y. Yan, B. Shang, S. Xu, and J. Tu, "An integrated CFD and machine learning analysis on pilots in-flight thermal comfort and productivity," Eng. Appl. Comput. Fluid Mech. **18**(1), 2421002 (2024).
[46]X. Li, X. Fang, and Y. Yan, "In-depth investigation of air quality and CO_2 lockup phenomenon in pilots' local environment," Exp. Comput. Multiphase Flow **6**(2), 170–179 (2024).
[47]C. Gui, F. Geng, J. Tang, H. Niu, C. Liu, H. Teng, X. Feng, S. Hu, and S. Li, "Spatial and temporal distribution of dust pollutants from a fully mechanized mining face under the improved air-curtain system," Powder Technol. **396**, 467–476 (2022).
[48]C. Gui, F. Geng, J. Tang, H. Niu, F. Zhou, C. Liu, S. Hu, and H. Teng, "Gas–solid two-phase flow in an underground mine with an optimized air-curtain system: A numerical study," Process Saf. Environ. Prot. **140**, 137–150 (2020).
[49]H. Wang, B. Jiang, H. Lin, H. Zheng, Y. Wang, B. Ji, and Y. Zhou, "Analysis of dust pollution characteristics in the respiratory risk zone of the roadway under multiple factors," Energy **305**, 132298 (2024).
[50]ANSYS Fluent, *Ansys Fluent Theory Guide* (Ansys Inc., 2011).
[51]X. Li, Z. Chen, J. Tu, H. Yu, Y. Tang, and C. Qin, "Impact of impinging jet ventilation on thermal comfort and aerosol transmission: A numerical investigation in a densely-occupied classroom with solar effect," J. Build. Eng. **94**, 109872 (2024).
[52]V. Akbari, T. N. G. Borhani, A. Shamiri, and M. S. Shafeeyan, "Computational fluid dynamics modeling of gas-solid fluidized bed reactor: Influence of numerical and operating parameters," Exp. Comput. Multiphase Flow **6**(2), 85–125 (2024).
[53]S. A. Morsi and A. J. Alexander, "An investigation of particle trajectories in two-phase flow systems," J. Fluid Mech. **55**(2), 193–208 (1972).
[54]F. Geng, G. Luo, Y. Wang, Z. Peng, S. Hu, T. Zhang, and H. Chai, "Dust dispersion in a coal roadway driven by a hybrid ventilation system: A numerical study," Process Saf. Environ. Prot. **113**, 388–400 (2018).
[55]Y. Feng, T. Marchal, T. Sperry, and H. Yi, "Influence of wind and relative humidity on the social distancing effectiveness to prevent COVID-19 airborne transmission: A numerical study," J. Aerosol Sci. **147**, 105585 (2020).
[56]Y. Yan, X. Li, X. Fang, Y. Tao, and J. Tu, "A spatiotemporal assessment of occupants' infection risks in a multi-occupants space using modified Wells–Riley model," Build. Environ. **230**, 110007 (2023).